

GRMHD SIMULATIONS OF VISIBILITY AMPLITUDE VARIABILITY FOR EVENT HORIZON TELESCOPE IMAGES OF SGR A*

LIA MEDEIROS^{1,2}, CHI-KWAN CHAN¹, FERYAL ÖZEL¹, DIMITRIOS PSALTIS¹, JUNHAN KIM¹,
DANIEL P. MARRONE¹, AND ALEKSANDER SĄDOWSKI³

Draft version October 30, 2021

ABSTRACT

Synthesis imaging of the black hole in the center of the Milky Way, Sgr A*, with the Event Horizon Telescope (EHT) rests on the assumption of a stationary image. We explore the limitations of this assumption using high-cadence GRMHD simulations of Sgr A*. We employ analytic models that capture the basic characteristics of the images to understand the origin of the variability in the simulated visibility amplitudes. We find that, in all simulations, the visibility amplitudes for baselines oriented perpendicular to the spin axis of the black hole typically decrease smoothly over baseline lengths that are comparable to those of the EHT. On the other hand, the visibility amplitudes for baselines oriented parallel to the spin axis show significant structure with one or more minima. This suggests that fitting EHT observations with geometric models will lead to reasonably accurate determination of the orientation of the black-hole on the plane of the sky. However, in the disk-dominated models, the locations and depths of the minima in the visibility amplitudes depend primarily on the width and asymmetry of the crescent-like images and are highly variable. In the jet-dominated models, the locations of the minima are determined by the separation of the two image components but their depths depend primarily on the relative brightness of the two components and are also variable. This suggests that using time-independent models to infer additional black-hole parameters, such as the shadow size or the spin magnitude, will be severely affected by the variability of the accretion flow.

Subject headings: accretion, accretion disks — black hole physics — Galaxy: center — radiative transfer

1. INTRODUCTION

The Event Horizon Telescope (EHT), a very long baseline interferometer (VLBI) experiment with baselines ranging from Arizona to California and from the South Pole to Europe, will, for the first time, be able to resolve black holes at horizon scales (see, e.g., Doeleman et al. 2009). This will not only allow us to test theories of accretion physics but will also give us an unprecedented look at general relativistic effects in the strong field regime (Psaltis & Johannsen 2011). Sagittarius A* (Sgr A*), the black hole at the center of our galaxy, is one of the primary targets for the EHT. It has a large angular size, a well constrained mass and distance (Ghez et al. 2008; Gillessen et al. 2009), and a broadband spectrum that has been studied for more than a decade (see Baganoff et al. 2001 and Genzel et al. 2003 for early studies).

The source-integrated monochromatic flux of Sgr A* has been observed to be variable at many wavelengths including at 1.3 mm, the wavelength at which the EHT will operate (e.g., Marrone et al. 2008; Porquet et al. 2008; Do et al. 2009). In a previous paper, we studied the large scale variability as a function of wavelength for the source-integrated monochromatic flux of Sgr A* (Chan et al. 2015a) and found two kinds of variability: long timescale flaring events and shorter timescale, persistent

variability originating from the turbulent flow.

Our simulations show that both long and short timescale variability occur at event horizon scales. The structure of the emission region, and therefore, the interferometric visibilities predicted by the simulations are highly variable. Current image reconstruction algorithms rely on the assumption that the black hole image remains stationary on typical observation timescales of a few hours. This means that the resulting image will actually be sampled from different realizations of the emission of Sgr A* and that the variability of Sgr A* must be taken into account when analyzing non-simultaneous data.

In this paper we aim to understand the effect of variability on the properties of the visibility amplitudes. To perform this analysis, we employ our GRMHD simulations with high spatial and time resolution, and long time span that were reported in Chan et al. (2015a,b). In the earlier paper, we made use of the fast ray tracing code `GRay` to efficiently integrate null geodesics in a curved space time and to calculate images, spectra, and lightcurves. Here, we calculate the visibilities at 1.3 mm for five best-fit models, which were chosen so that their average broadband spectra and image sizes at 1.3 mm match observations. We employ analytic models to understand the behavior and significance of various features in the visibility amplitudes and use our simulations to investigate the ability of analytic models to capture the gross features of the black-hole images.

2. THE GRMHD+RAY TRACING SIMULATIONS

In previous papers, we explored a variety of GRMHD+ray tracing simulations for the accretion flow

¹ Steward Observatory and Department of Astronomy, University of Arizona, 933 N. Cherry Ave., Tucson, AZ 85721

² Department of Physics, Broida Hall, University of California Santa Barbara, Santa Barbara, CA 93106

³ MIT Kavli Institute for Astrophysics and Space Research, 77 Massachusetts Ave, Cambridge, MA 02139

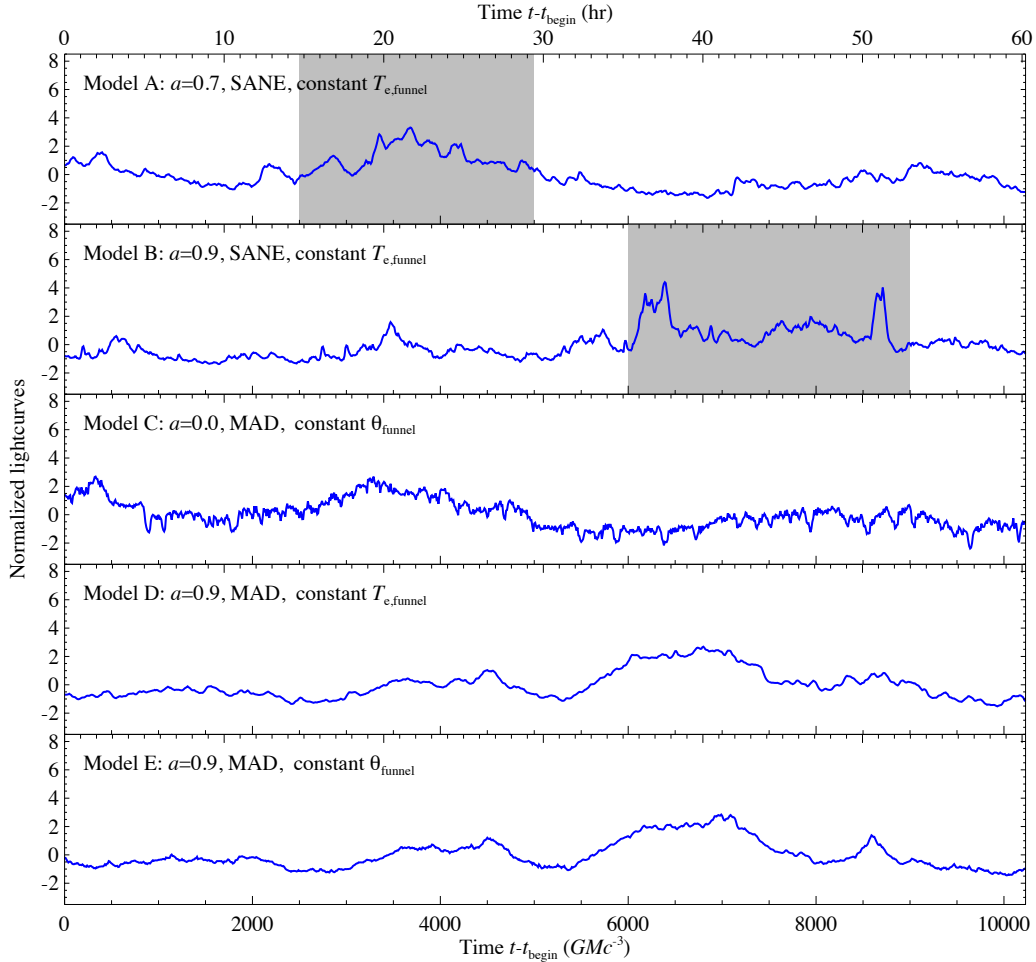


Figure 1. The 1.3 mm flux as a function of time for the five simulations we explore in this paper (see Chan et al. 2015a,b). Models A and B, the SANE models, have significant flaring events, shown in grey, which we have excluded from all calculations of averages throughout the paper. The models have a time resolution of $10 M$, which is approximately equal to 212 s for the mass of Sgr A* and a total duration of ≈ 60 hours.

around Sgr A* (Chan et al. 2015b). These models were created using HARM (Narayan et al. 2012; Sądowski et al. 2013) for the GRMHD simulations and GRay (Chan et al. 2013) for solving the radiative transfer equation along null geodesics. We used simulations with a time resolution of $10 GMc^{-3}$, where G is the gravitational constant, $M = 4.3 \times 10^6 M_{\odot}$ is the mass of Sgr A*, and c is the speed of light. For the remainder of this paper we employ gravitational units and set $G = c = 1$.

We explored a large range of physical conditions by varying the black hole spin ($a=0$ to 0.9), the accretion rate, the magnetic field configuration, and the thermodynamic prescriptions for the electrons used in the plasma models. Specifically, we explored initial magnetic field configurations that led to Standard And Normal Evolution (SANE) as well as to Magnetically Arrested Disk (MAD) flows (Narayan et al. 2012). Out of a large number of simulations, we identified five models which best fit the time averaged observations of Sgr A* (Chan et al. 2015b). The specific criteria we used to constrain these models are (a) a flux and a slope at 10^{11} – 10^{12} Hz that matches observations, (b) a flux at $\simeq 10^{14}$ Hz that falls within the observed range of the highly variable infrared

flux, (c) an X-ray flux that is consistent with 10% of the observed quiescent flux, i.e., the percentage which has been attributed to emission from the inner accretion flow (Neilsen et al. 2013), and (d) a size of the emission region that is consistent with the size determined by the early EHT observations (Doeleman et al. 2008).

Figure 1 shows the light curves for the five models we consider in this paper. These light curves were calculated by computing the source integrated monochromatic flux from each model for 1024 late-time snapshots for a total duration that corresponds to 60 hrs for the assumed black hole mass. Models A and B have SANE flows and the same plasma model but differ on the choice of black hole spin: Model A has $a = 0.7$, while Model B has $a = 0.9$. Both models A and B show large amplitude, short timescale variability that was shown to be consistent with broadband observations in Chan et al. (2015a). Models D and E have the same black hole spin of $a = 0.9$ and the same MAD configuration, but differ on the choice of the plasma model used. Both models D and E show only long timescale, low amplitude variability. Model C consists of a MAD flow and a black hole spin of $a = 0$. Model C shows very fast, quasi-periodic, low amplitude

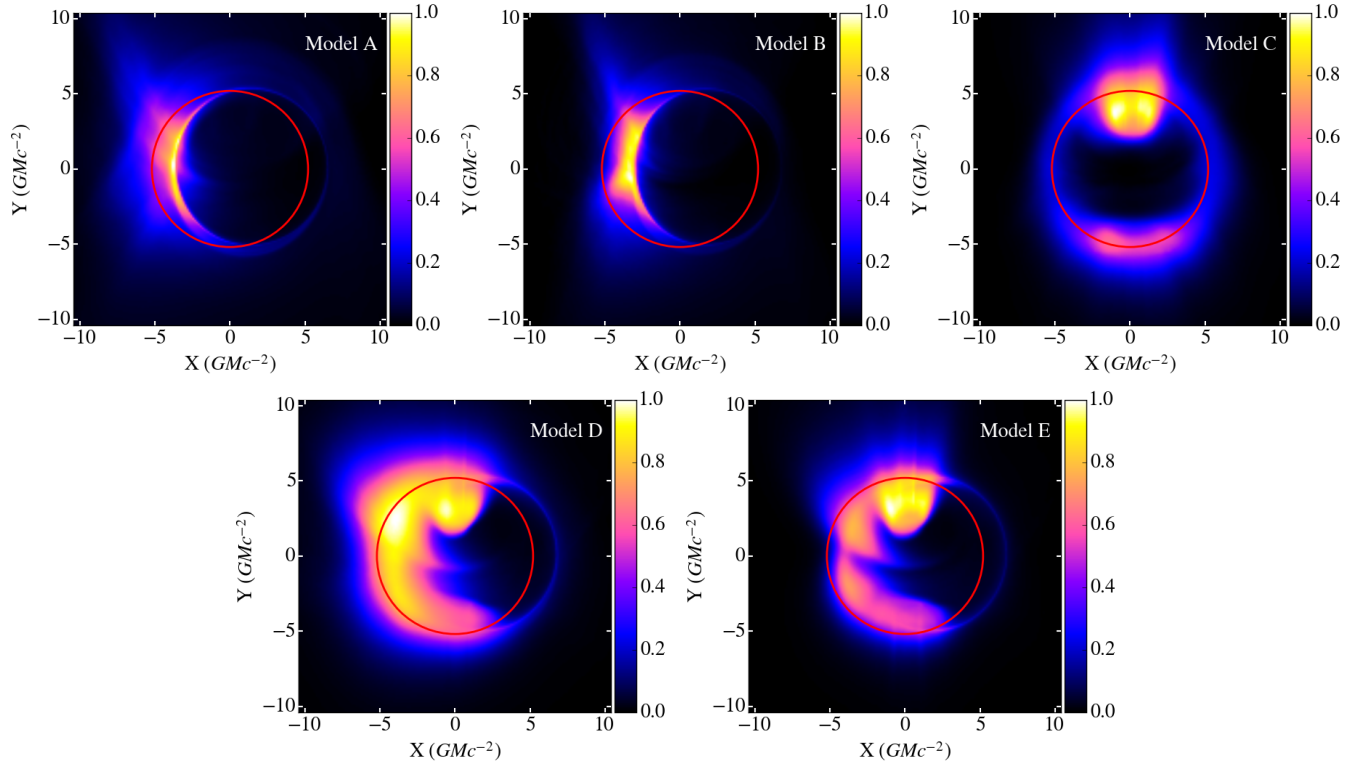


Figure 2. The average 1.3 mm images of the five models we consider in this paper. The SANE models (A and B) have most of their emission originating from the disk region, while the MAD models (C, D, and E) have significant emission originating from the jets. Model C is unique, with a black hole spin of zero, which results in an almost symmetric image without the Doppler beaming effects that are present in the other models. The red circles indicate the expected size of the black hole shadow according to general relativity. The maximum intensity in each panel has been normalized to unity.

variability.

In order to focus on the persistent variability from the turbulent flow, we ignore hereafter the intervals with large flaring events, shown in grey in Figure 1. These events were already discussed in Chan et al. (2015a).

Figure 2 shows the average 1.3 mm images for the five models we consider. The SANE models (A and B) show a mostly connected emission region and appear to have their emission dominated by the disk. Models C and E on the other hand show disconnected emission regions and have most of their emission originating from the bases of the jets. Model D is a hybrid with a bright peak at the base of the jet (as in Models C and E) as well as a crescent shape (as in A and B). The red circles in the figures have a radius of $\sqrt{27}M$, i.e., the expected shadow radius of a non-rotating black hole according to general relativity. The images of the black hole shadow for models A, B, D, and E appear shifted to the right and have most of their emission originating from the left side due to Doppler beaming in a Kerr metric. The black hole shadow for model C is not shifted from the center and is much more symmetric than the others because the black hole spin in this model is zero.

Although Figure 2 shows resolved images of Sgr A* at 1.3 mm, the EHT is an interferometer and will measure the complex Fourier components of Figure 2. To explore the properties of the actual observables, we show in Figure 3 the average 1.3 mm visibility amplitudes for the five models. We calculated these visibility amplitudes by performing, on each snapshot, the two dimensional

Fourier transform

$$V(u, v) = \iint I(\alpha, \beta) e^{-2\pi i(u\alpha + v\beta)} d\alpha d\beta, \quad (1)$$

where $\alpha \equiv X/D$, $\beta \equiv Y/D$, and D is the distance to Sgr A*, and then taking the mean magnitude of the complex Fourier components. The white lines are the current and planned tracks of the various baselines of the EHT shown for a particular N-S orientation of the black hole (see, e.g., Doeleman et al. 2009). The visibility amplitude maps of models A and B appear elongated in the horizontal direction. This is because the Fourier transform is the conjugate of the original image and the original image is a crescent elongated in the vertical direction. Models C, D, and E show multiple emission peaks in the original image along the vertical direction. This results in multiple peaks in the visibility amplitude maps, along the same axis. Model C appears to be more symmetric in both the original image and its transform.

3. TIME DEPENDENCE OF VISIBILITIES

Even though the visibility maps shown in Figures 3 allow us to identify the gross features of the images, they do not faithfully represent the observations that the EHT will obtain. As discussed in the introduction, the EHT relies on the rotation of the Earth to increase its coverage of the $u - v$ plane and, therefore, make a better image. However, Sgr A* is variable on timescales that are much shorter than a day. We now aim to quantify the effect of variability on the structure of the visibility amplitude.

3.1. SANE Models

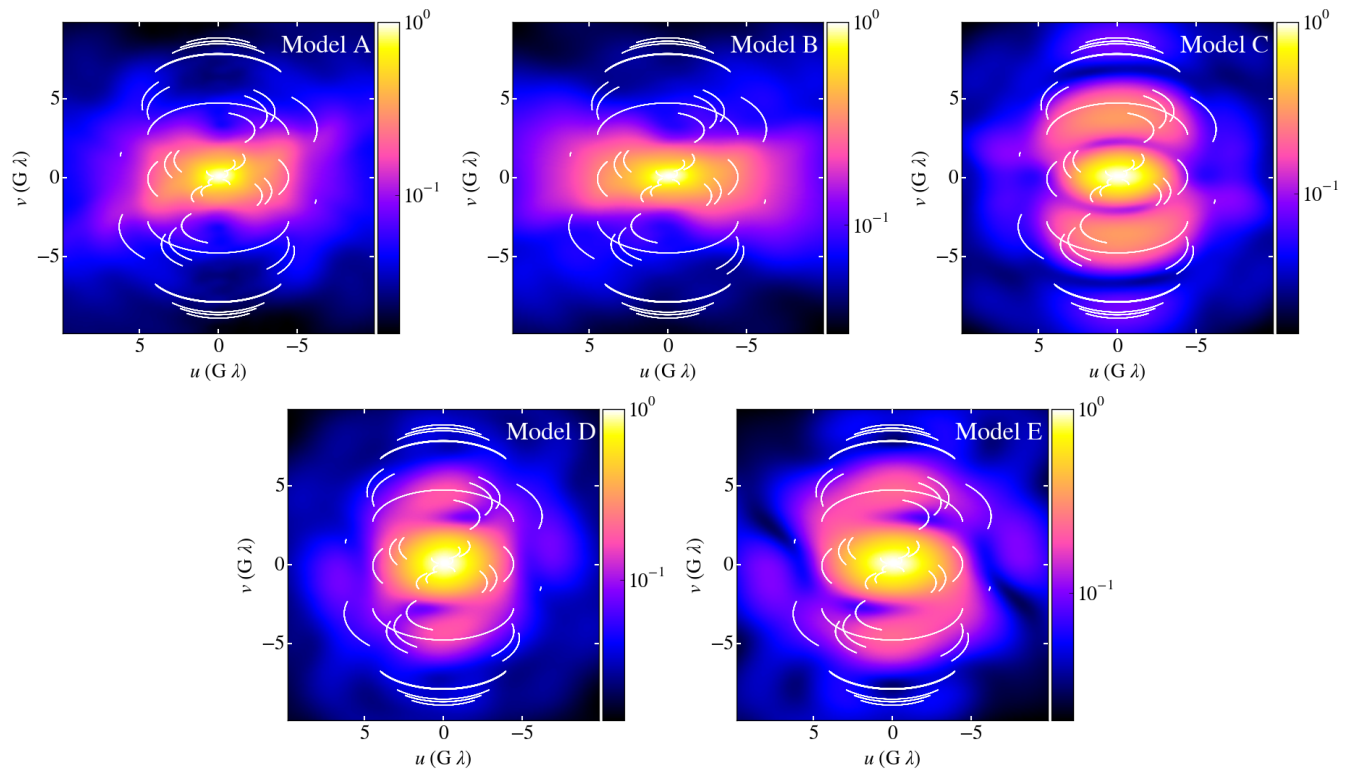


Figure 3. The average 1.3 mm visibility amplitudes, calculated by taking the magnitudes of the complex Fourier components of the two dimensional Fourier transforms, of each snapshot of the five simulations shown in Figure 1 and then averaging over the snapshots. The white lines denote the current and future tracks of the EHT baselines as the Earth rotates. Baselines are shown for an arbitrary N-S black hole orientation for illustrative purposes only. The maximum visibility amplitude in each panel has been normalized to unity.

The SANE models A and B have their 1.3 mm emission structure dominated by the disk and have crescent-like shapes. In Figures 4 and 5, we show the mean simulated images, the means of the visibility amplitudes of each snapshot, and the visibility amplitudes of the mean simulated images, for these SANE models. Comparing the mean visibility amplitudes to the visibilities of the mean images reveals an expected but important consequence of variability. The visibilities of any snapshot (including of the average image) have significantly more structure than the average visibilities.

To explore the behavior of the structure of visibility amplitudes further, we turn our focus to the images from the individual snapshots. In the various panels of Figure 6, we show (a) the simulated images, (b) the projections of these images along directions parallel and perpendicular to the black hole spin axis, (c) the visibility amplitudes, and (d) the cross sections of the visibility amplitudes taken along directions parallel and perpendicular to the black hole spin axis for 5 snapshots from model B. The projection-slice theorem states that the Fourier transform of the projection of a two-dimensional image onto some axis is equal to a slice of the Fourier transform of the image as long as the slice is parallel to the projection axis and intersects the center of the visibility amplitude map. As a result, the cross sections of the visibility amplitudes shown in the rightmost panels are just the one-dimensional Fourier transforms of the projections shown in the second column of panels.

In the rightmost column, we see that the visibility amplitude cross sections perpendicular to the spin axis de-

crease slowly and smoothly while those parallel to the spin axis have a lot more structure. Particularly, the cross sections parallel to the spin axis often have minima, but the location and depth of these minima are variable. By taking the average of the visibility amplitudes, we lose all information about the minima and are left with a smoothly decreasing visibility amplitude, as was seen in the mean of the visibilities in Figures 4 and 5.

To understand the behavior described above, we employ a simple analytic model to represent the properties of the emission regions. Since the SANE models (A and B) have their emission dominated by the Doppler boosted disk, it roughly resembles a crescent shape. Following Kamruddin & Dexter (2013), we use a model of an asymmetric ring, defined as the difference between two offset disks with different radii, which becomes a crescent as its asymmetry grows. The diagram in Figure 7 shows the parameters used to describe our asymmetric ring model. The Fourier transform of the asymmetric ring is given by

$$V_{\text{cres}}(k) = \frac{2\pi I_0 R_1}{k} \left[J_1(R_1 k) - e^{-2\pi i(\alpha_0 u)} R J_1(k R_2) \right], \quad (2)$$

where $k \equiv 2\pi\sqrt{u^2 + v^2}$, J_1 are Bessel functions of the first kind, I_0 is the constant surface brightness of the disks, α_0 is the displacement of the smaller disk from the center of the larger disk in the α direction, and $R = R_2/R_1$. Hereafter, we set $R_1 = 1$ without loss of generality. We also define the widths of the asymmetric ring on the left and right sides of the image as

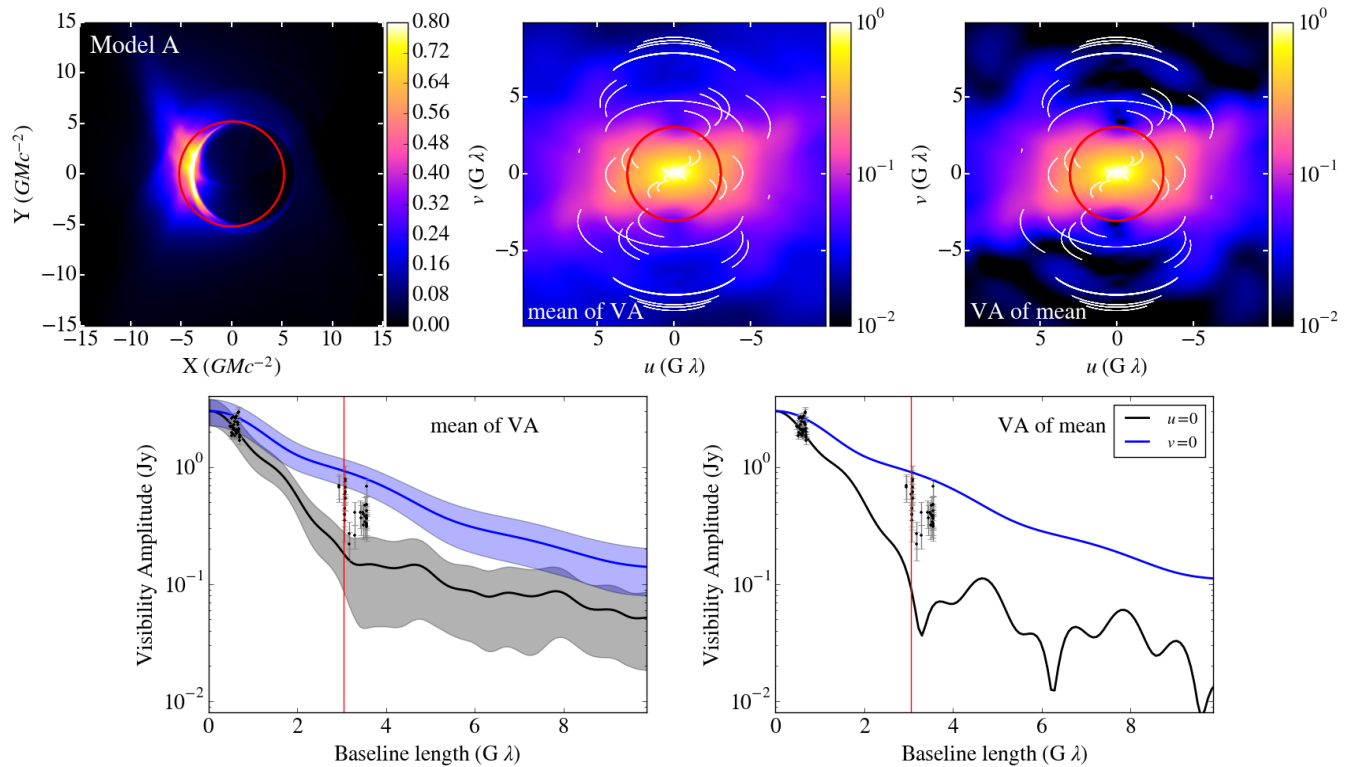


Figure 4. (Top Left) Mean simulated image of Model A. Red circle indicates the location of the black hole shadow. (Top Middle) Mean of the visibility amplitude of each snapshot. Red circle indicates the first null in the visibility amplitude of a thin photon ring located at the radius of the black hole shadow. (Top Right) Visibility amplitude of the mean simulated image. Red circle is the same as the top middle panel. (Bottom Left) Cross sections, taken parallel (black line and region) and perpendicular (blue line and region) to the black hole spin axis, of the top middle panel. These cross sections were not chosen to correspond to any particular EHT baselines. The colored regions are the 68% ranges of the mean visibilities at each baseline. Red line is the location of first null in the visibility amplitude of a thin photon ring located at the radius of the black hole shadow. (Bottom Right) Cross sections, taken parallel (black line and region) and perpendicular (blue line and region) to the black hole spin axis, of the top right panel. The red line is the same as the bottom left panel. The black points and grey error bars in the bottom panels are EHT data taken in 2007 and 2009 shown here for illustrative purposes only (Doeleman et al. 2008, Fish et al. 2011).

$w_l \equiv R_1 - R_2 + \alpha_0$ and $w_r \equiv R_1 - R_2 - \alpha_0$.

A cross section of the visibility amplitudes parallel to the black hole spin axis is then given by

$$V_{\text{cres}, u=0}(v) = \frac{I_0}{v} [J_1(2\pi v) - R J_1(2\pi R v)], \quad (3)$$

which only depends on R , the ratio of the two radii, and not on α_0 , the displacement of the smaller disk. In other words, the visibility amplitude along the directions parallel to the spin axis will be the same regardless of the asymmetry of the ring. For an infinitesimally thin ring, i.e., when $w_l \ll R_1$ and $w_r \ll R_1$, the visibility amplitude along a direction parallel to the spin axis has a minimum at $u \simeq 0.4/R_1$. However, Figure 8 shows that changing the width of the ring, $w_l = w_r = R_1 - R_2$, changes the location of the minima. In the SANE simulations (A and B) the width of the approximately crescent shape is highly variable because of different turbulent structures appearing and disappearing from the Doppler boosted side of the crescent. This is why the location of the minima are also highly variable.

The cross section of the visibility function perpendicular to the spin axis of the black hole ($v = 0$) is equal

to

$$V_{\text{cres}, v=0}(u) = \frac{I_0}{u} [J_1(2\pi u) - e^{-2\pi i \alpha_0 u} R J_1(2\pi R u)]. \quad (4)$$

Although the visibility amplitude of a cross section parallel to the spin axis did not depend on the displacement α_0 , which measures the asymmetry of the ring, the perpendicular cross section does. Figure 9 shows the dependence of the visibility amplitude on the degree of asymmetry of the ring w_r/w_l . As the ring becomes more asymmetric, i.e., as $w_r/w_l \rightarrow 0$, the visibility amplitude of the cross section perpendicular to the spin axis becomes smoother and all traces of minima are lost. Due to the effects of Doppler beaming, our simulations are completely dominated by one side of the ring. This is why the cross sections of the visibilities perpendicular to the spin axis (e.g., the blue curves in Figures 4 and 5) are broad and monotonically decreasing, while the parallel cross sections have strong local minima.

The model described above cannot fully encompass all of the variable structure that we see in Figure 6. In the GRMHD simulations, the emission is not always a simple crescent. In some snapshots, the emission along the equatorial plane gets blocked by the colder disk which causes the emission to have two disjointed regions. When this occurs, the visibility amplitudes have short-lived features

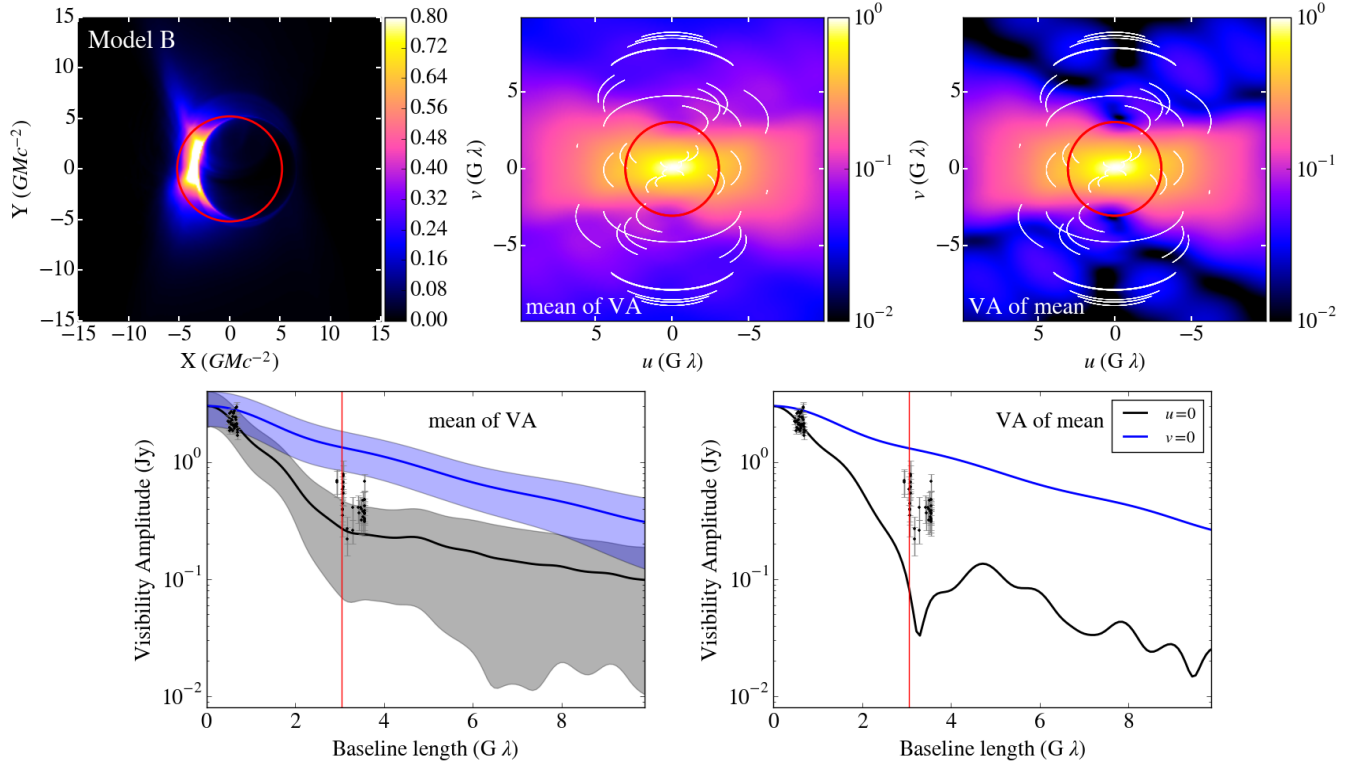


Figure 5. Same as Figure 4, but for Model B.

similar to those of the MAD models, which have two disjointed peaks of emission and will be discussed below.

In summary, for most instances, the behavior of the SANE models (A and B) can be roughly modeled by an asymmetric ring of variable width. The behavior of the cross section of the visibility amplitude that is parallel to the spin axis does not depend on the asymmetry of the ring and exhibits minima. The location of these minima depends on the width of the asymmetric ring, which is variable. Because of this variability, taking the average of the visibility amplitude over time will result in a visibility amplitude with reduced or no minima. The direction perpendicular to the spin axis, however, does depend on α_0 . An extremely offset ring, where the thinnest part has a thickness of zero, has a monotonically decreasing visibility amplitude.

3.2. MAD Models

The 1.3 mm emission of the MAD models (C, D, and E) is dominated by the funnels and jet footprints; because of this, it is characterized broadly by two peaks. Throughout the simulations, the relative widths and amplitudes of the peaks change but the distance between them remains approximately constant since it is set by the size of the black hole shadow.

Figures 10 and 11 are the equivalent of Figure 4 but for Models C and D, respectively. Focusing on the one-dimensional cross sections of the visibility amplitude of the mean and the mean of the visibility amplitudes, the cross sections perpendicular to the spin axis have less pronounced minima, which are located at baselines much larger than expected for the size of Sgr A*. The cross sections parallel to the spin axis show much more pronounced minima, close to the expected location for the

size of Sgr A*, much like the SANE models. Unlike the SANE models, however, the means of the visibility amplitudes and the visibility amplitudes of the means have very similar structures and both have a minimum in the vertical direction. Furthermore, the minima appear to be in the same locations and the ranges of amplitudes at a given baseline are much smaller than those of the SANE models. This indicates that the existence and location of a visibility minimum is more persistent in MAD models than in SANE models.

To understand the behavior of the MAD models, we employ an approximate model of their emission using two Gaussians separated by a distance d in the direction parallel to the spin axis but with no separation in the direction perpendicular to the spin axis. We define this model as (see Figure 12)

$$I(\alpha) = A_1 e^{-[(\alpha - \alpha_{01})^2 / 2\sigma_{\alpha 1}^2 + (\beta - \beta_{01})^2 / 2\sigma_{\beta 1}^2]} + A_2 e^{-[(\alpha - \alpha_{02})^2 / 2\sigma_{\alpha 2}^2 + (\beta - \beta_{02})^2 / 2\sigma_{\beta 2}^2]}. \quad (5)$$

To simplify our notation, we set $\alpha_{01} = \beta_{01} = 0$ such that one Gaussian is peaked at the origin; set $\alpha_{02} = 0$ so that the Gaussians are separated by a distance $d = \beta_{02}$ along the β axis, and define the ratio of amplitudes $A \equiv A_2 / A_1$. This reduces to an overall normalization of A_1 , which we ignore to get

$$I(\alpha) = e^{-[\alpha^2 / 2\sigma_{\alpha 1}^2 + \beta^2 / 2\sigma_{\beta 1}^2]} + A e^{-[\alpha^2 / 2\sigma_{\alpha 2}^2 + (\beta - d)^2 / 2\sigma_{\beta 2}^2]}. \quad (6)$$

We further define the quantities

$$\alpha' \equiv \frac{\alpha}{\sigma_{\alpha 1}}, \quad \sigma'_{\alpha} \equiv \frac{\sigma_{\alpha 2}}{\sigma_{\alpha 1}}, \quad \beta' \equiv \frac{\beta}{\sigma_{\beta 1}}, \\ \sigma'_{\beta} \equiv \frac{\sigma_{\beta 2}}{\sigma_{\beta 1}}, \quad d' \equiv \frac{d}{\sigma_{\beta 1}}, \quad (7)$$

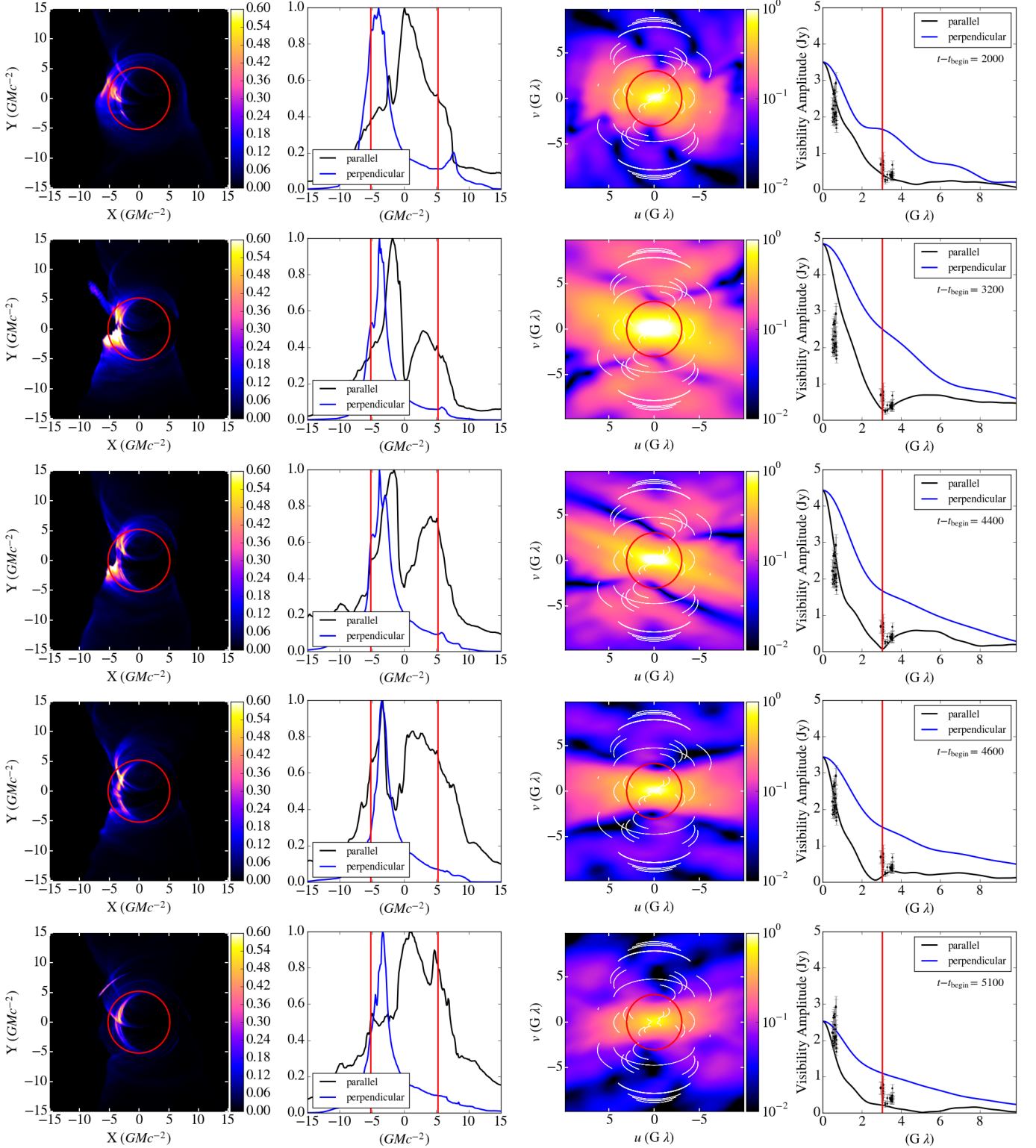


Figure 6. Example snapshots from Model B. From left to right: the simulated image for each snapshot, the projections of the simulated image in directions parallel and perpendicular to the black hole spins axis, the visibility amplitude for this snapshot, and the cross sections for the visibility amplitude of this snapshot.

which in turn gives

$$\begin{aligned}
 I(\alpha) &= e^{-(\alpha'^2 + \beta'^2)/2} + Ae^{-(\alpha'^2/\sigma'_\alpha + (\beta' - d')^2/\sigma'_\beta^2)/2} \\
 &= e^{-(\alpha^2 + \beta^2)/2} + Ae^{-(\alpha^2/\sigma_\alpha + (\beta - d)^2/\sigma_\beta^2)/2}. \quad (8)
 \end{aligned}$$

In this last expression, we omitted the primes for clarity. We now take the Fourier transform of the intensity to

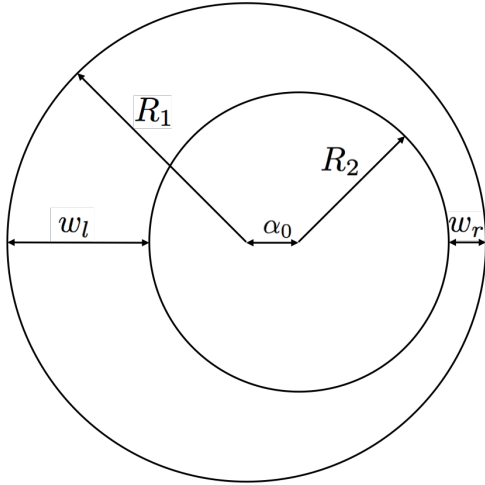


Figure 7. An analytic representation of an asymmetric ring model (following Kamruddin & Dexter 2013) as a difference between two offset disks with different radii.

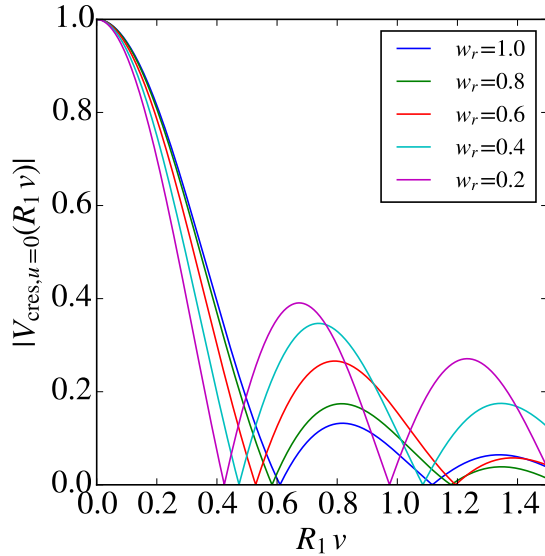


Figure 8. The cross section of the visibility amplitude which is parallel to the spin axis for the analytic asymmetric ring model for different widths of the ring. Since the parallel cross section does not depend on the asymmetry of the ring, we have set $w_l = w_r$. A characteristic null appears in the visibility amplitude at $v \approx 0.5/R_1$, with its precise location depending on the width of the ring.

obtain

$$V_{2g}(k) = 2\pi e^{-(u^2+v^2)2\pi^2} + 2\pi A \sigma_\alpha \sigma_\beta e^{-(u^2\sigma_\alpha^2 + v^2\sigma_\beta^2)2\pi^2} e^{-2\pi i d v}. \quad (9)$$

The visibility along a direction parallel to the spin axis takes the form

$$V_{2g, u=0}(v) = 2\pi e^{-2(\pi v)^2} + 2\pi A \sigma_\alpha \sigma_\beta e^{-2(\pi \sigma_\beta v)^2} e^{-2\pi i d v}. \quad (10)$$

Its magnitude, $|V_{2g}(v)|$, has a minimum when $V_{2g}(v)$ is minimum, i.e., when the second term is real and negative. This occurs when

$$vd = (2n + 1)/2, \quad (11)$$

i.e., the location of the minimum depends only on the

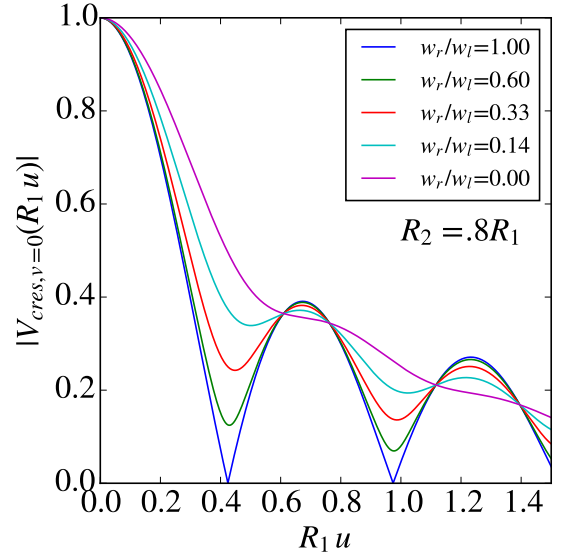


Figure 9. The cross section of the visibility amplitude in the direction perpendicular to the spin axis for the asymmetric ring model, for different degrees of asymmetry in the ring brightness. As the ring becomes more asymmetric, the local minimum at $u \approx 0.5/R_1$ becomes less pronounced.

separation between the two Gaussians and not on any of their other properties. Note that, in this configuration, the location of the minimum occurs at a baseline length that is different compared to the case of an asymmetric ring model (see Figures 10 and 11). This minimum will reach zero when the amplitudes of the two terms in the sum are equal, or when

$$A = \frac{1}{\sigma_\alpha \sigma_\beta} e^{-\pi^2(1-\sigma_\beta^2)(2n+1)^2/2d^2}. \quad (12)$$

The simplified analytic model shows that two Gaussians do not always produce a null in the visibility amplitude. For a given separation d and width ratios σ_α and σ_β , there is only one value of the ratio of the brightness of the two Gaussians, A , that gives rise to a null. When a local minimum does not reach zero, the properties of the two components of the image affect the depth of the minimum. This is shown in Figure 13 for the dependence of the depth of the minimum on the ratio A of the brightness of the two components of the image and, in Figure 14, for the dependence of the ratio of widths of the two components along the spin axis of the black hole. In our MAD simulations, the relative amplitudes and widths of the two peaks is highly variable; however, the distance between the two peaks remains approximately constant and is set by the size of the black hole shadow. Because of this, the depth of the minimum varies but the location is approximately constant. When we average minima of various depths but constant location, we get a minimum in the same location of an average depth.

The cross sections of the visibility amplitude maps perpendicular to the spin axis do not exhibit nulls. Analytically, the perpendicular cross sections of the visibility amplitudes of two Gaussians separated in the vertical direction is given by

$$V_{2g, v=0}(u) = 2\pi e^{-2(\pi u)^2} + 2\pi A \sigma_\alpha \sigma_\beta e^{-2(\pi \sigma_\alpha u)^2}, \quad (13)$$

which is just the addition of two Gaussians both peaked

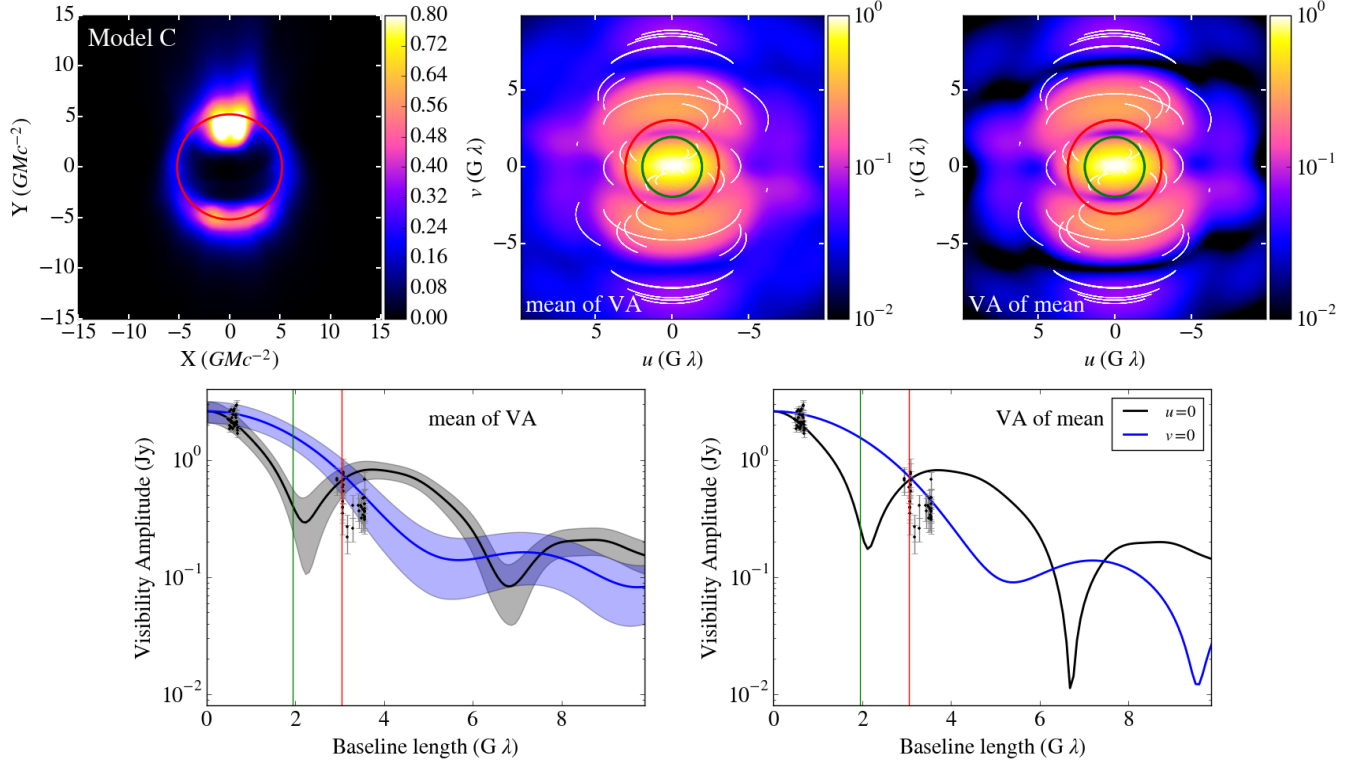


Figure 10. Same as Figure 4, but for the images from Model C and with the addition of green circles in the top middle and right panels and green lines in the bottom panels. The location of these corresponds to the location of the first minimum in the visibility amplitude of two Gaussians separated by a distance equal to the size of the black hole shadow. These minima occur at small baseline lengths compared to the minima of the asymmetric ring shown in red.

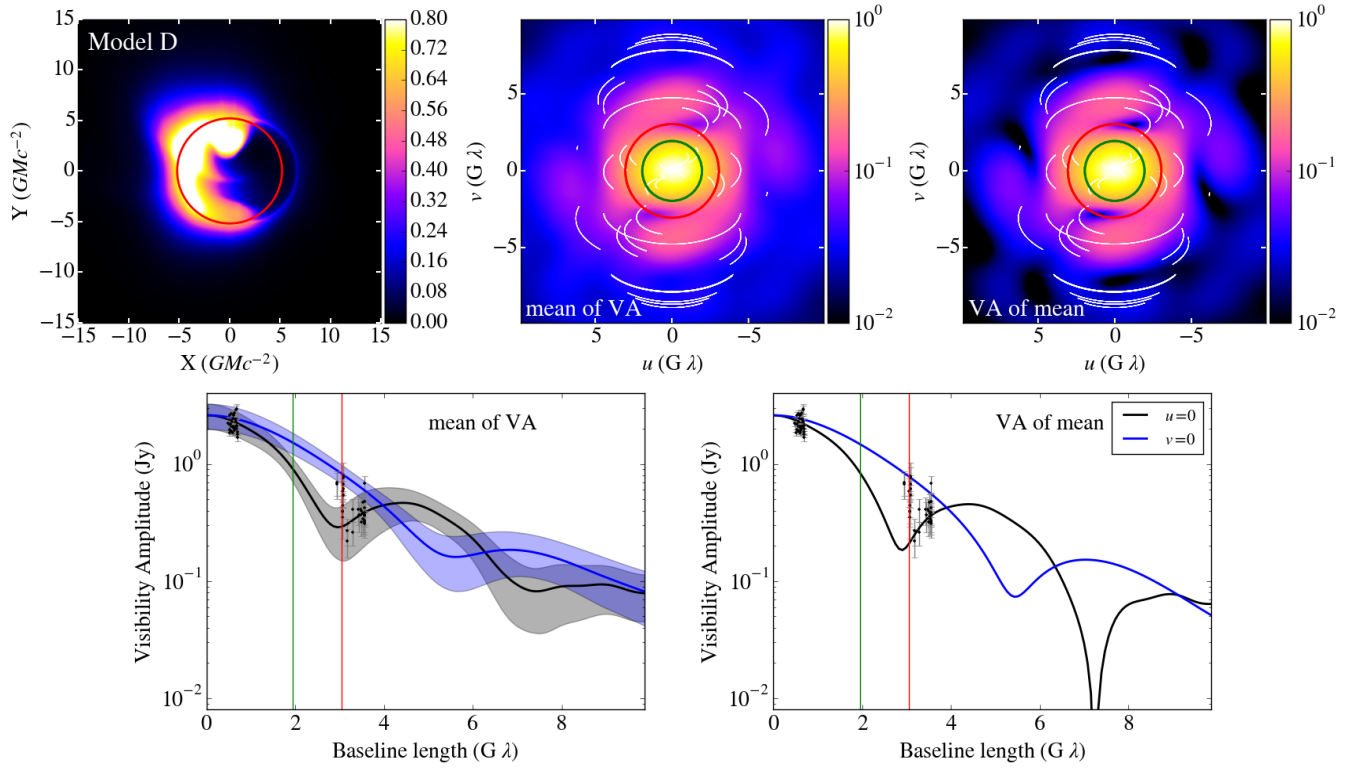


Figure 11. Same as Figure 10, but for Model D.

at the origin, and therefore has no nulls.

In our simulations, the visibility amplitudes of the

MAD models have a consistent minimum in the direction parallel to the spin axis of the black hole. The location

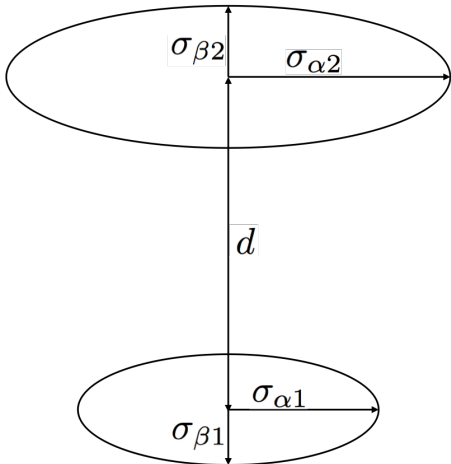


Figure 12. An analytic representation of a two spot model in terms of two Gaussian components separated by a distance d along the vertical direction.

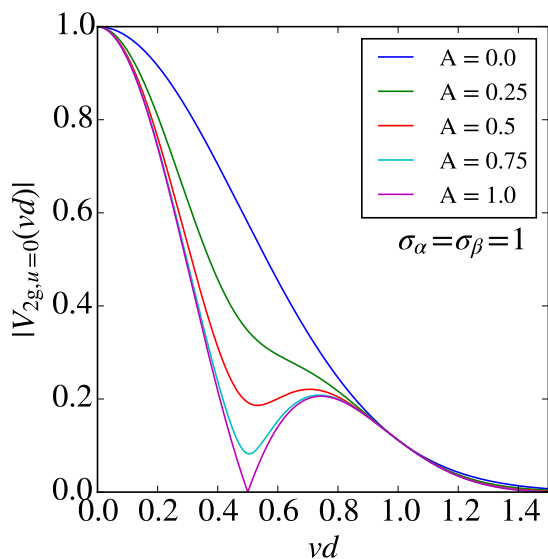


Figure 13. The cross section of the visibility amplitude in the direction parallel to the spin axis, for the analytic two-component model for different relative brightnesses of the components, A . We have also set the displacement to $d = 3$ and the relative widths to $\sigma_\alpha = \sigma_\beta = 1$. The baseline dependence of the visibility amplitude shows a characteristic minimum at a location that depends only on the distance between the two components of the image. The minimum becomes deeper as the relative brightness of the two components becomes equal to unity.

of the minimum is approximately constant and is determined primarily by the size of the black hole shadow. Averaging over time does not appear to erase the minimum as it did in the SANE models.

4. CONCLUSIONS

In this paper, we quantified the effect of MHD turbulence driven variability on the structure of visibility amplitudes of the upcoming imaging observations of Sgr A* with the EHT. We explored the effect of variability on the structure of the emission region in order to understand the challenges that variability will pose for image reconstruction of EHT observations. We created and analyzed mock data using GRMHD simulations, that were con-

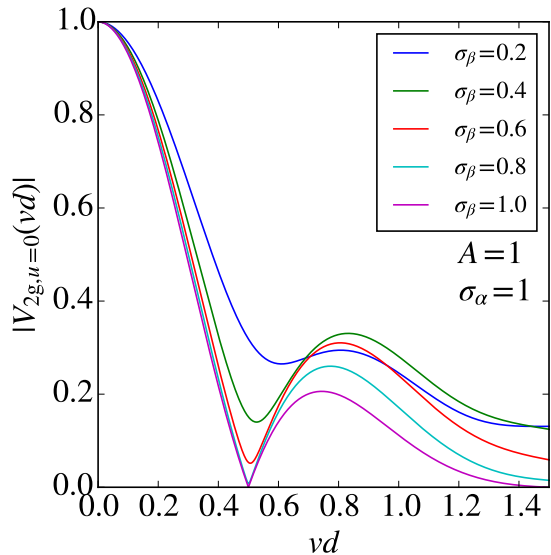


Figure 14. The cross section of the visibility amplitude in the direction parallel to the spin axis, for the analytic two-component model for different widths of the components, σ_β . We have also set the displacement to $d = 3$, the relative widths in the α direction to $\sigma_\alpha = 1$, and the relative brightnesses to $A = 1$. As in Figure 13, the visibility amplitudes show a characteristic minimum around $v = 0.5/d$. The minimum becomes deeper as the relative width of the two components of the image becomes one.

strained in previous work such that their time averaged properties and 1.3 mm image size match observations of Sgr A*.

We found that the visibility amplitude of the SANE models resembles that of a highly asymmetric ring. The width of the asymmetric ring is highly variable due to the turbulent accretion flow. The visibility amplitude in the direction parallel to the spin axis of the black hole typically exhibits minima with locations that depend on the width of the asymmetric ring. Since the location of the minima in the direction parallel to the spin axis depends on the width of the emitting region, and is therefore variable, any information that could be inferred by the presence of a minimum is lost by averaging over time.

The SANE models rarely exhibit minima in the direction perpendicular to the spin axis of the black hole. The reason for this is that due to Doppler beaming the majority of emission comes from the left of the spin axis, with negligible emission coming from the right. This asymmetry does not affect the visibility amplitude in the direction parallel to the spin axis, but affects the depth of minima in the direction perpendicular to the spin axis. For the perpendicular direction, a highly asymmetric ring has a visibility amplitude that decreases monotonically.

In contrast, the images and visibility amplitudes of the MAD models are characterized by two bright spots at the footpoints of the jets, separated by a relatively constant distance equal to the size of the black hole shadow. For the MAD models, the visibility amplitudes in the direction parallel to the spin axis have persistent nulls in constant locations but with variable depths. The locations of the minima in the direction parallel to the spin axis of MAD models depend strongly on the separation between the two image components. Since the distance between the emission peaks in our simulations are set

primarily by the size of the black hole shadow and are approximately constant, the location of the minimum is constant. However, varying the widths, or amplitudes, of the image components affects the depths of the minima. On the other hand, the visibility amplitudes in the direction perpendicular to the spin axis have much less pronounced minima at larger baselines.

Our results strongly suggest that fitting early EHT data using simple models of the accretion flow that do not take into account its intrinsic variability will lead to a reasonably accurate determination of the orientation of the black-hole spin on the plane of the sky that will depend only weakly on the flow properties (see, e.g., Broderick et al. 2011; Psaltis et al. 2015). This is true because, in both the disk-dominated SANE models and the jet-dominated MAD models, the visibility amplitudes perpendicular to the spin axes are smoother and vary over longer baselines while the visibilities along the spin axes have significantly more structure and drop faster with baseline length. However, using such models to measure more detailed properties of the black hole, such as the size of its shadow and the magnitude of its spin will be severely hampered by the variability in the flow. For example, the spin of the black hole affects primarily the widths of the crescent-like shapes of disk-dominated images and, hence, the locations and depths of minima in the visibility amplitudes. However, turbulence in the accretion flow causes both the locations and depths of these minima to be highly variable, effectively masking the effect of black-hole spin on the image. In order for the EHT observations to lead to accurate determination of the black-hole shadow size and spin, the image reconstruction and model fitting algorithms will need to take into account the variability of the underlying images explicitly.

We thank Ramesh Narayan for collaborative work that led to this paper and for helpful comments and sugges-

tions on the manuscript. L.M. acknowledges support from NFS GRFP grant DGE 1144085. C.K.C., F.O., and D.P. were partially supported by NASA/NSF TCAN award NNX14AB48G and NSF grants AST 1108753 and AST 1312034. J.K., and D.M. acknowledge support from NSF grant AST-1207752 and AST-1440254. All ray tracing calculations were performed with the *E1 Gato* GPU cluster at the University of Arizona that is funded by NSF award 1228509.

REFERENCES

- Baganoff, F. K., Bautz, M. W., Brandt, W. N., et al. 2001, *Nature*, 413, 45
- Chan, C.-k., Psaltis, D., & Özel, F. 2013, *ApJ*, 777, 13
- Chan, C.-k., Psaltis, D., Özel, F., et al. 2015a, *ApJ*, 812, 103
- Chan, C.-K., Psaltis, D., Özel, F., Narayan, R., & Sądowski, A. 2015b, *ApJ*, 799, 1
- Do, T., Ghez, A. M., Morris, M. R., et al. 2009, *ApJ*, 691, 1021
- Doeleman, S., Agol, E., Backer, D., et al. 2009, in *Astronomy, Vol. 2010, astro2010: The Astronomy and Astrophysics Decadal Survey*
- Doeleman, S. S., Weintroub, J., Rogers, A. E. E., et al. 2008, *Nature*, 455, 78
- Fish, V. L., Doeleman, S. S., Beaudoin, C., et al. 2011, *ApJ*, 727, L36
- Genzel, R., Schödel, R., Ott, T., et al. 2003, *Nature*, 425, 934
- Ghez, A. M., Salim, S., Weinberg, N. N., et al. 2008, *ApJ*, 689, 1044
- Gillessen, S., Eisenhauer, F., Trippe, S., et al. 2009, *ApJ*, 692, 1075
- Kamruddin, A. B., & Dexter, J. 2013, *MNRAS*, 434, 765
- Marrone, D. P., Baganoff, F. K., Morris, M. R., et al. 2008, *ApJ*, 682, 373
- Narayan, R., Sądowski, A., Penna, R. F., & Kulkarni, A. K. 2012, *MNRAS*, 426, 3241
- Neilsen, J., Nowak, M. A., Gammie, C., et al. 2013, *ApJ*, 774, 42
- Porquet, D., Grosso, N., Predehl, P., et al. 2008, *A&A*, 488, 549
- Psaltis, D., & Johannsen, T. 2011, *Journal of Physics Conference Series*, 283, 012030
- Sądowski, A., Narayan, R., Penna, R., & Zhu, Y. 2013, *MNRAS*, 436, 3856